

Molecular Physics



An International Journal at the Interface Between Chemistry and Physics

ISSN: 0026-8976 (Print) 1362-3028 (Online) Journal homepage: https://www.tandfonline.com/loi/tmph20

Formation of argon cluster with proton seeding

O. C. F. Brown, D. Vrinceanu, V. Kharchenko & H. R. Sadeghpour

To cite this article: O. C. F. Brown, D. Vrinceanu, V. Kharchenko & H. R. Sadeghpour (2020): Formation of argon cluster with proton seeding, Molecular Physics, DOI: 10.1080/00268976.2020.1767813

To link to this article: https://doi.org/10.1080/00268976.2020.1767813



Taylor & Francis Taylor & Francis Group

RESEARCH ARTICLE



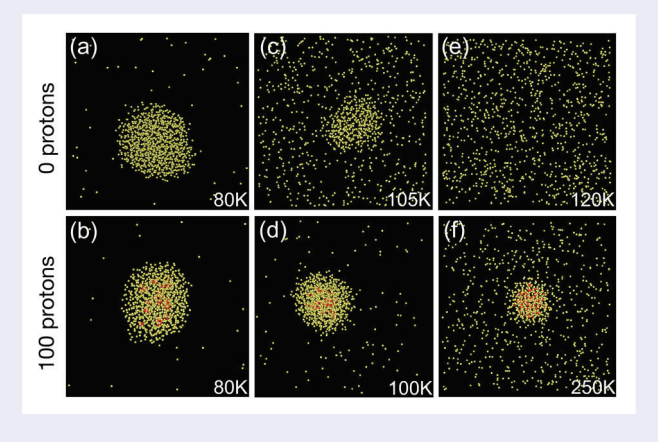
Formation of argon cluster with proton seeding

O. C. F. Brown^{a,b}, D. Vrinceanu ^{oc}, V. Kharchenko^{a,d} and H. R. Sadeghpour ^{oa}

^aITAMP, Harvard-Smithsonian Center for Astrophysics, Cambridge, MA, USA; ^bDepartment of Physics and Astronomy, University of Southampton, Southampton, UK; ^cDepartment of Physics, Texas Southern University, Houston, TX, USA; ^dDepartment of Physics, University of Connecticut, Storrs, CT, USA

ABSTRACT

We employ force-field molecular dynamics simulations to investigate the kinetics of nucleation to new liquid or solid phases in a dense gas of particles, seeded with ions. We use precise atomic pair interactions, with physically correct long-range behaviour, between argon atoms and protons. Time dependence of molecular cluster formation is analysed at different proton concentration, temperature and argon gas density. The modified phase transitions with proton seeding of the argon gas are identified and analysed. The seeding of the gas enhances the formation of nano-size atomic clusters and their aggregation. The strong attraction between protons and bath gas atoms stabilises large nano-clusters and the critical temperature for evaporation. An analytical model is proposed to describe the stability of argon-proton droplets and is compared with the molecular dynamics simulations.



ARTICLE HISTORY

Received 17 February 2020 Accepted 7 May 2020

KEYWORDS

Cluster formation; molecular dynamics simulations; protonated argon gas

1. Introduction

Gas phase clusters are weakly bound aggregates comprised of either atoms or molecules, and often display chemical and physical properties that are quite distinct from those of their atomic constituents or associated bulk materials [1,2]. To synthesise catalysts or thin films, size-selected gas clusters can be delivered to substrates to obtain materials with desired individual or collective properties [3,4]. Thermodynamics of gas phase clusters, aerosols and clouds bears on the nature of nanoparticle formation in the atmosphere and in the interstellar medium [2].

Recent interest in optical and physical properties of gas phase clusters has been partly stimulated by the discovery of exoplanets and analysis of absorption and emission spectra of their hazy atmospheres. Optical and infrared spectra observed from planetary and exoplanetary atmospheres, comets, and natural satellites are sometimes unusually featureless, which are attributed to the presence of atmospheric dust, ice, haze and aerosol particles [5–7]. Haze is mostly formed by small (submicron) cluster particulates that can produce a broad continuum opacity to light. Interaction between haze particles and radiating atoms or molecules can dramatically modify

♠ Supplemental data for this article can be accessed here. https://doi.org/10.1080/00268976.2020.1767813

absorption spectra of exoplanets [5,8-11] and used as markers for the simulation of atmospheric constituents. Recent laboratory experiments simulating hazy environments for super-Earths and mini-Neptunes atmospheres suggest that some of these atmospheres contain thick photochemically generated hazes [12].

Compositions and parameters of haze particle and atmospheric gases are expected to vary considerably for different exoplanets. The most realistic atmospheric haze materials are water and CO2 ice and liquid droplets for the terrestrial atmospheres and methane or hydrocarbons for the Jupiter-type exoplanets and Titan [13]. Investigation of the haze formation in most important atmospheric gases, such as CO2, H2O, CH4, is a formidable task due to a complexity of molecular quantum interaction in polyatomic gases. Cluster formation in noble gases represents an ideal environment for the laboratory simulations and theoretical modelling of spectral changes induced by ultra-small haze particles and aggregates.

Argon is a potential target species in search for naturally occurring, noble gas compounds. Argon is known to be polarisable with the proper ligands [14]. While argon clusters are some of the simplest chemical systems to study, experimental investigations of the structure and stability of neutral rare-gas clusters and nano-size liquid droplets are extremely challenging. Charged clusters are on the other hand, easily studied using mass spectrometric techniques [15,16]. The first noble gas molecule observed in nature is the simple argon-proton cation (argonium, Ar-p) [17]. Argonium has been detected in the interstellar medium (ISM) toward various astronomical objects [18,19]. Also, the existence of the protonbound dimer Ar-p-Ar has been proved by spectroscopic evidence in argon matrix [20,21]. Ion-molecule complexes of the form Ar_np are detected in pulsed-discharge supersonic expansions containing hydrogen and argon [22] and studied theoretically [23]. The nucleation stimulated by proton seeding is unique because proton has no core electrons, and from the chemical point of view it can be seen as a point charge [24].

Considerable effort has been devoted to obtaining a better understanding of the nucleation [25,26], structural properties [27], collision dynamics [28] and phase transitions [29,30] of argon clusters by means of classical Molecular Dynamics (MD) [31]. The dependence of argon phase transformations on the size of clusters is investigated experimentally by using electron diffraction analysis [32-34] and was predicted theoretically using MD simulations [35]. Phase diagram of argon nanoclusters up to 400 atoms has been reported by means of constant energy molecular dynamics simulations [36].

The cluster nucleation in atomic and molecular gases occurs in several stages. Phase transitions from

a thermodynamically metastable state to a stable state occur in the homogeneous gas due to microscopic fluctuations. Fluctuations produce nano-size clusters in a liquid or solid phase. These clusters are relatively stable and become centres of growth of a new phase, if the typical cluster size R is larger than some critical value R_c . Clusters with $R < R_c$ are unstable and disappear back into the gas phase [37]. Ions and other seed particles may stimulate the formation of critical clusters arising in the early stage of nucleation. Modelling of production of critical clusters is the most difficult part in investigations of nucleation processes. We performed MD simulations aimed at clarifying the kinetics of short-term nucleation, which initiates sub-critical and critical clusters. The longterm stages of haze formation, such as coalescence, when growth of larger clusters occurs due to 'swallowing up' of small ones [37], can then described with standard kinetics of the first order phase transition.

Charge particles can catalyse short-term cluster formation in the gas phase. A main goal of this work is to study argon nucleation with and without proton seeding, based on the most accurate quantum-mechanical binary potentials for classical MD simulations. We will show how small concentrations of positive ions accelerate nucleation process, but high ionic densities prevent the formation of the gas phase clusters. The phase transitions in clusters due to the temperature change and proton contribution are studied by analysing the pair correlation functions (the radial distribution function -RDF) and the size of nucleation clusters. Other order parameters, or discriminating quantities such as mean square displacement, or diffusion coefficient, are more adapted to studying bulk transformations because their dependence on cluster size makes these parameters less unique. In future extensions of this work for larger clusters and aggregates, these complementary measures will be investigated.

2. Simulation procedure and details

The Large Atomic/Molecular Massively Parallel Simulator (LAMMPS) [38] is employed to perform simulations of the dynamics of cluster formation in an Ar gas when seeded with protons. The classical force fields are calculated from the quantum mechanical pair interaction potentials which are described in detail below. The results are visualised using Visual Molecular Dynamics software (VMD) [39].

2.1. Binary interaction potentials

The dynamics of cluster formation, stability and structural properties with ion seeding are obtained from MD simulations that use classical force fields deduced from

Ar–Ar interaction. The binary Ar–Ar potential is modelled by a Lennard-Jones 6-12 (LJ) potential [36,40,41].

$$V_{Ar-Ar}(r) = 4\varepsilon \left[\left(\frac{\sigma}{r} \right)^{12} - \left(\frac{\sigma}{r} \right)^{6} \right], \tag{1}$$

where parameters, $\varepsilon = 1.23 \times 10^{-2} \text{ eV}$ and $\sigma = 3.357 \text{ Å}$, are deduced from gas and matrix spectroscopy. The physically correct weak van der Waals (vdW) asymptotic behaviour is evident from the LJ potential.

Ar-p interaction. The Ar-p Born-Oppenheimer (BO) potential energy curves for the ground and excited electronic states were calculated by Sidis [42]. The BO potentials were subsequently used for the calculations of the scattering phase shifts and compared with existing experimental data, which in turn used to improve the well depth of the ab initio results.

The long-range form of the Ar-p energy is dominated by the polarisation potential Equation (5), due to the polarisability of the Ar ground state. This long-range potential (region III) is connected to the BO potential at intermediate and short-range (region I), by a switching function (region II).

At short distances, the Ar-p energy is modelled by a Morse-type potential as [42],

$$V_{\text{Ar}-p}^{(I)}(r) = U \times (x^2 - 2x),$$
 (2)

with

$$x = \left(\frac{r_e}{r}\right)^a e^{[b(r_e - r)]} \tag{3}$$

where $U = 4.3 \text{ eV}, r_e = 1.34 \text{ Å}, \text{ and},$

$$a = 0.475$$
, $b = 1.370 \,\text{Å}^{-1}$ when $r < 1.34 \,\text{Å}$ $a = 0.400$, $b = 1.890 \,\text{Å}^{-1}$ when $r > 1.34 \,\text{Å}$

The switching function is defined in the interval [3.6 Å, 3.86 Å] (region II) as,

$$V_{\text{Ar}-p}^{(II)}(r) = \frac{A}{e^{\gamma(r-r_s)} + 1} + B \times r + C,$$
 (4)

where $A = -0.095 \,\text{eV}$, $B = 0.01 \,\text{eV/Å}$, $C = -0.085 \,\text{eV}$, $\gamma = 7.0 \,\text{Å}^{-1}$ and $r_s = 3.5 \,\text{Å}$. The Ar-p interaction potential at long range is given by

$$V_{\text{Ar}-p}^{(III)}(r) = -\frac{q_p^2 \alpha}{8\pi \varepsilon_0 r^4},$$
 (5)

where $\alpha = 11.08 a_0^3$ is the argon static polarisability in the ground state, q_p is the ionic charge in a charge neutral plasma, ε_0 is the permittivity of free space, and a_0 is the atomic unit of length.

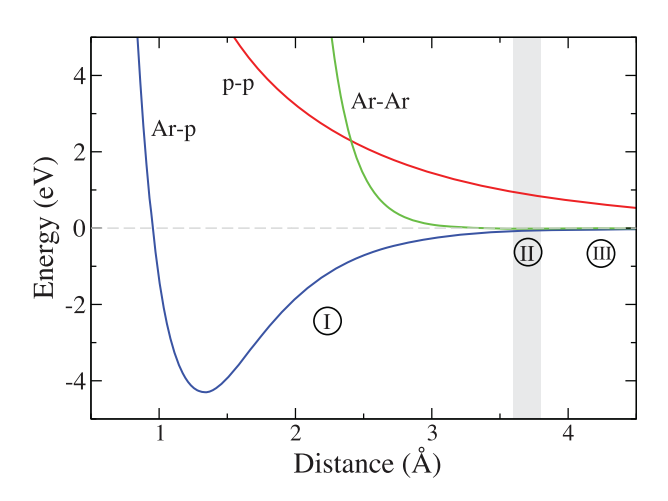


Figure 1. Potential energy curves of pair interactions for the MD simulations. The Ar-Ar interaction (green) is modelled by LJ potential, Equation (1). The screened proton–proton potential Equation (6) (red) is calculated at a particular density with $\lambda_D =$ 2.5 Å using the Debye shielding feature available in LAMMPS. The potential energy between argon atoms and protons (blue) is defined in short (I) and long (III) ranges, with a switching function connecting them in region (II), Equations (2)–(5).

p–p interaction. The Coulomb repulsion between two protons is shielded in a neutral plasma by the free electrons. This is modelled by Debye shielding feature available in LAMMPS. The Debye length is [43],

$$\lambda_D = \sqrt{\frac{\varepsilon_0 k_B}{q_p^2 \left(\frac{\rho_e}{T_e} + \frac{\rho_p}{T_p}\right)}},\tag{6}$$

where k_B is the Boltzmann constant, T_p and T_e are the temperatures of the ions and electrons respectively, ρ_p and ρ_e are the ion and electron number densities, respectively. The screened potential is

$$V_{p-p}(r) = \frac{q_p^2}{4\pi\varepsilon_0 r} e^{-r/\lambda_D}.$$
 (7)

The interaction potentials are displayed in Figure 1. While the Ar-Ar BO potential contains a shallow well in the region II and is asymptotically attractive due to long range vdW forces, the greatest attraction in the simulations is understandably due to the Ar-p potential in region I. The competition between the screened p-pand Ar-p interactions ultimately determines the formation and stability of the clusters as a function of proton concentration.

2.2. MD simulations

Each MD simulation starts by generating random coordinates for a given number of atoms and ions, with a minimum separation of 3 Å. Simulations are performed with a fixed number of Ar atoms (1000) and a variable number of protons, from 0 to 100, while adjusting the simulation cell in order to obtain various densities. The simulations are performed with the canonical (NVT) ensembles with a Nosé-Hoover thermostat [38].

Since the Debye length depends on temperature, simulations are run at various temperatures with adjusted Debye length. Charge neutrality in the simulation cell is preserved by specifying an equal number of electrons and protons in Equation (6).

We are interested in the short-time dynamics of Ar and Ar–*p* cluster nucleations. Experimentally, the proton seeding could be implemented by selective laser ionisation of H atoms in the Ar and H gas mixture. Energies of photo-electrons can be significantly larger than the bath gas temperature. Energy relaxation of electrons occurs mostly in collision with the Ar atoms and the electron plasma thermalisation requires significantly more time than the characteristic time of cluster formation. For example, electrons with energies around 11.5 eV can form the long-living metastable ions $Ar^{-}(3p^{5}4s4p)$ with the lifetime \sim 260–300 ns [44]. This time is much larger than a time of $\sim 10 \, \text{ns}$ required for the production of critical clusters. Energetic electrons do not play a significant role in Debye screening and, aside from providing the plasma neutrality, they are not material to the simulations.

The average time between collision of atomic particles $\tau_{col} = 1/(\rho_{Ar}\sigma_{Ar}\langle v \rangle)$ has to be significantly larger than the simulation time step, δt . Simple but realistic assumptions for the radius of Ar atoms $r_{\rm Ar} \sim 10^{-8} \, {\rm cm}$ and for the elastic cross section of Ar-Ar collisions, $\sigma_{\rm Ar}$ \sim πr_{Ar}^2 allow us to estimate τ_{col} at the argon number density of $\rho_{\rm Ar}=10^{21}\,{\rm cm}^{-3}$, and an average velocity $\langle v\rangle\sim$ $10^4\,\mathrm{cm\,s^{-1}}$, as $au_{col}\sim 0.3$ ns. We therefore use a fine timestep of $\delta t = 1.0$ fs $\ll \tau_{col}$ for all the simulations here. For our simulations, this time resolution is always less than the collision time and therefore gives us the capability to observe the dynamics at high densities. To determine the number of atoms in a cluster, the distance between atoms were evaluated during the simulation and any that were within 6 Å of each other were counted to be part of a single cluster. This distance was chosen based on the lattice constant of the Ar crystal, $a = 5.26 \,\text{Å}$ [45]. Dispersed small clusters eventually aggregate to form one large cluster at longer times.

3. Results and discussion

3.1. Ar solid phase transition without proton seeding

We first study the crystallisation of argon at a high density, without proton seeding. This process of the cluster

formation is an excellent example of homogeneous nucleation [37]. The simulations are performed at high densities of Ar atoms $\rho_{\rm Ar}\sim 10^{22}~{\rm cm}^{-3}$ and $T=40~{\rm K}$. This density is achieved by positioning 1000 argon atoms regularly in a cube at 4.62 Å separation. At this density, $\langle r \rangle \sim \rho_{\rm Ar}^{-1/3} \sim 10~{\rm Å} > \sigma$. At such mean separations, the Ar atoms are ensured on average, to experience each other through the attractive vdW interactions. It can therefore be predicted that the system quickly transforms into a solid phase, which can have an amorphous or polycrystalline structure.

The inset in Figure 2 shows the final configuration of this system after 10 ns of MD simulation. This crystalline and/or amorphous structure is compared with the perfect fcc argon crystal that has atoms separated by precise distances. A meaningful measure of phase transition is the radial distribution functions (RDF), presented in Figure 2 and computed as,

$$g_{ab} = \frac{\langle \rho_b(r) \rangle}{\langle \rho_b \rangle_{loc}} \tag{8}$$

where $\langle \rho_b(r) \rangle$ refers to the average density of particle b at a distance r from particle a and $\langle \rho_b \rangle_{loc}$ refers to the density of the particles b, as if they are uniformly distributed within the simulation cell.

Figure 2 demonstrates the formation of an amorphous/crystalline structure during the simulation. The peaks represent particle densities distributed around their respective bulk lattice positions indicated by the vertical dashed lines labelled by the irrational multiples ($\sqrt{2}$, $\sqrt{3}$, ...) of the inter Ar atom equilibrium separation parameter, $\sigma_m = 2^{1/6}\sigma$ [46].

The height of the vertical bars are proportional to the coordination numbers corresponding to the ideal crystal positions and inversely proportional to the square of their distances. The shape of the RDF curve follows roughly the same pattern, with maxima around lattice separations. The agreement is qualitative and is affected by thermal motion, finite size of the sample and large surface effects, explaining for example why the RDF is non-zero in between ideal crystal sites. The spherical-like shape of final configuration depends on the way of building the starting configuration, although the RDF curves are stable, and only depend on the temperature and the number of particles.

3.2. Phase transition with proton seeding

Argon in the gas phase is normally monoatomic [47]. The weak interatomic interactions between Ar atoms is manifested in Ar low normal melting $T_m \simeq 83.8 \,\mathrm{K}$ [48] and boiling $T_b = 87.28 \,\mathrm{K}$ [49] temperatures. This behaviour can be predicted from an analysis of Ar–Ar interatomic

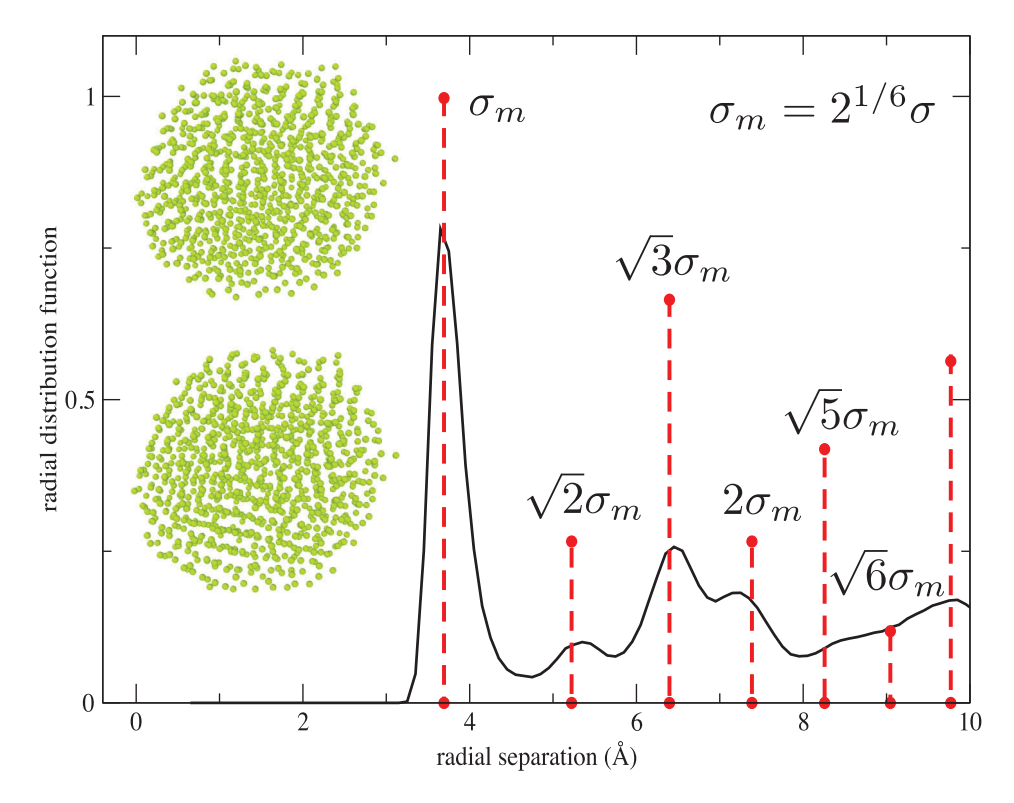


Figure 2. The Ar-Ar RDF of pure solid argon cluster formed from initial density of 10²² cm⁻³ after 10 ns of MD simulation at 40 K. The inset shows snapshots of atom configuration from two different viewpoints. The bottom cluster viewpoint in the inset shows more clearly the lattice structure. The vertical dashed lines indicate the coordination spheres of the ideal FCC crystal labelled by irrational multiples of the LJ parameter $\sigma = 3.357$ Å. The height of the vertical lines are the coordination numbers scaled by the square of the corresponding radius of coordination sphere, and normalised to unity for the σ_m peak.

potential that has a shallow attractive well and a steep repulsive wall, as shown in Figure 1.

To examine the phase transition of argon, simulations are performed at 10²¹ cm⁻³ argon density in a simulation cell with length of 100 Å at T = 50 K. Phase diagram of pure argon [50] indicates that the system at this point is still in the solid phase. The simulation is run for 10 ns to ensure that a single solid phase cluster of all the atoms has formed at the steady-state condition. The size of clusters are then monitored as the temperature gradually increases until clusters no longer exist. The results are shown in Figure 3. The red curve, for instance, in the absence of protons, shows temperatures up to $T = 200 \,\mathrm{K}$, and a transition from the solid to the gas phase at a temperature between $T=80-120\,\mathrm{K}$. Transitions from the crystalline solid state to gas phase can occur via intermediate amorphous or liquid cluster states. These phases have been detected by analysing the radial pair correlation functions. This can also be seen clearly from the snapshots of the system given in the top panels in Figure 4(a-d).

The proton seeding effect on the cluster formation is investigated by increasing the proton density in the MD simulation box. The results are illustrated in Figure 3 when $N_p = 5$, 10, 20, 50, 100 protons are randomly added to the simulation cell which already has 1000 randomly positioned argon atoms.

The most prominent feature in Figure 3 is the appearance of a distinct plateau with proton seeding. This plateau indicates the formation of a stable liquid phase. The reader is referred to the pair-correlation functions in Figure 5 for a clear demonstration of the liquid phase plateau. The phase modification with proton seeding is observed as the liquid-Ar plateau widens with increasing proton number, and the solid phase melting point moves to higher temperatures with increasing proton number. The effectiveness of the seeding process on cluster formation and its stability can also be seen in the inset of Figure 3. As will be discussed in more details later (in Section D), this figure shows that the proton mediated nucleation and clustering makes the liquid-gas transition to linearly shift to higher temperatures with respect to N_p . Relatively strong attraction between protons and Ar atoms, see Figure 1, creates a favourable conditions for the Ar clustering and protons work as a strong 'ionic glue' for Ar atoms. Nevertheless, one should expect that at very high proton densities Coulomb's repulsion between ions will stimulate cluster decay.

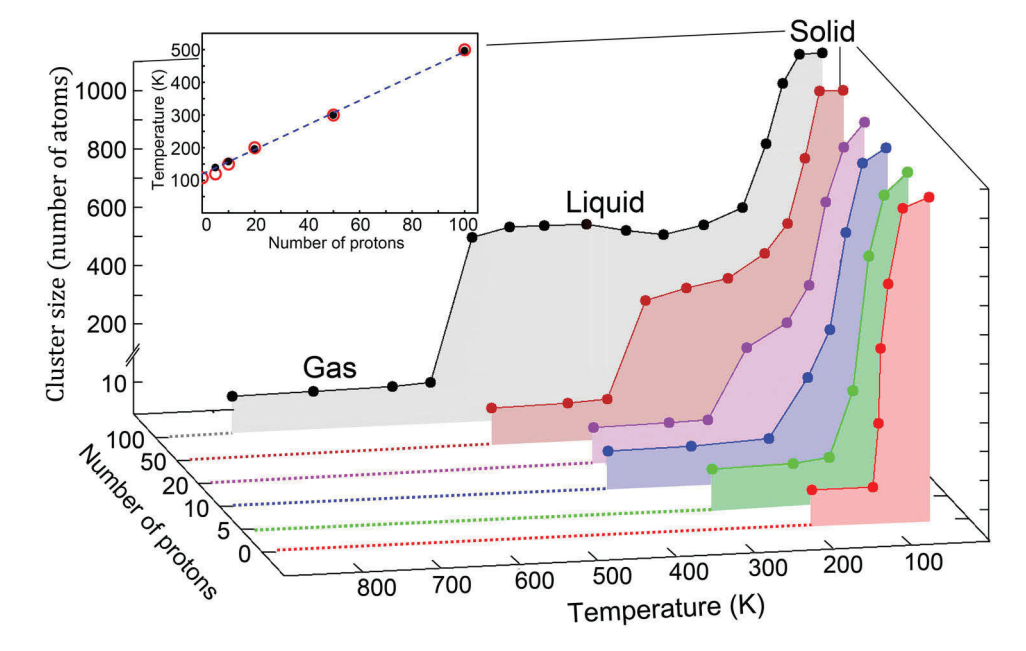


Figure 3. The average size of clusters plotted against temperature with various number of protons, N_p , when the initial argon density is 10^{21} cm⁻³. The inset shows the highest temperature, T_{crit} , at which stable clusters still exist, for each of the simulated systems. The red empty circles are from the MD simulations, and the solid black circles are predictions from Equation (10).

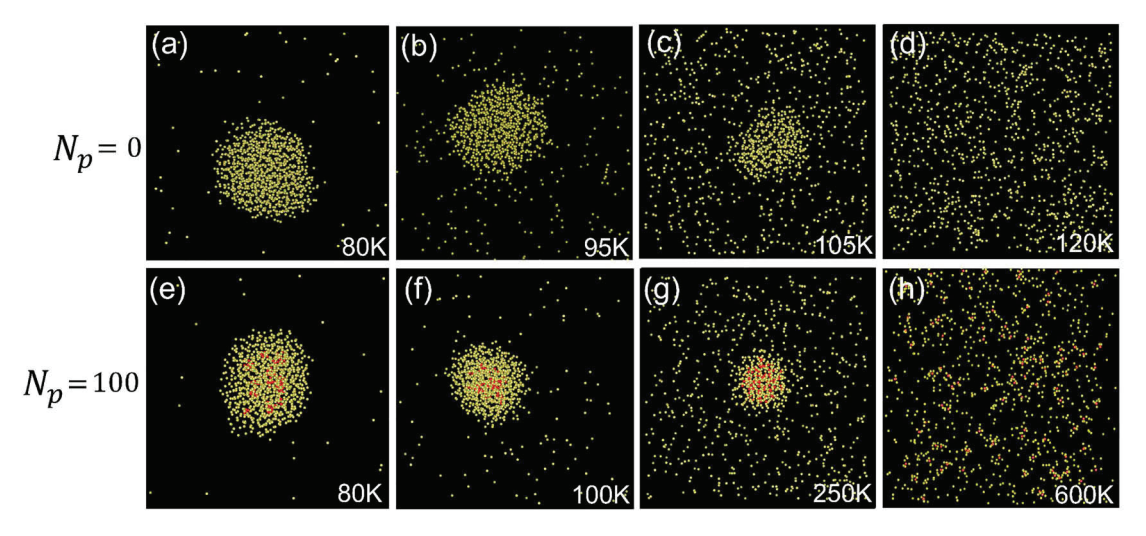


Figure 4. Snapshots of clusters formed without protons (top panels, a–d) and with 100 protons (bottom panels, e–h). The argon density is 10^{21} cm⁻³. Particles coloured in red are protons, whilst yellow particles are argon atoms. Up to the critical temperature, T_{crit} , less than 10% of protons are found outside the clusters.

The snapshots in the bottom panels in Figure 4(e–g) visualise the formation of the droplets at a proton density of $\rho_p=10^{20}~\rm cm^{-3}$ at higher temperatures. The transition to the gas phase in this case happens at $T>500~\rm K$, Figure 4(h). As can be seen from the plateau in Figure 3, the size of clusters in the liquid phase, at temperatures T=200–500 K, stays roughly constant, i.e. around 500 argon atoms. By measuring the volume of these clusters, the Ar number density of the droplets is calculated to be $\sim 1.2 \times 10^{21}~\rm cm^{-3}$.

3.3. Radial distribution function analysis

The pair-correlation radial distribution function (RDF) analysis is performed to confirm the nature of the phases at different temperatures. Figure 5(a) shows the Ar–Ar RDF curves for at $T=20\,\mathrm{K}$ (solid), $T=250\,\mathrm{K}$ (liquid) and $T=600\,\mathrm{K}$ (gas). The curves exhibit characteristic signatures for corresponding phases with temperature [51]. The relatively periodic and discrete peaks in the blue curve at $T=20\,\mathrm{K}$ demonstrate the coordination shell

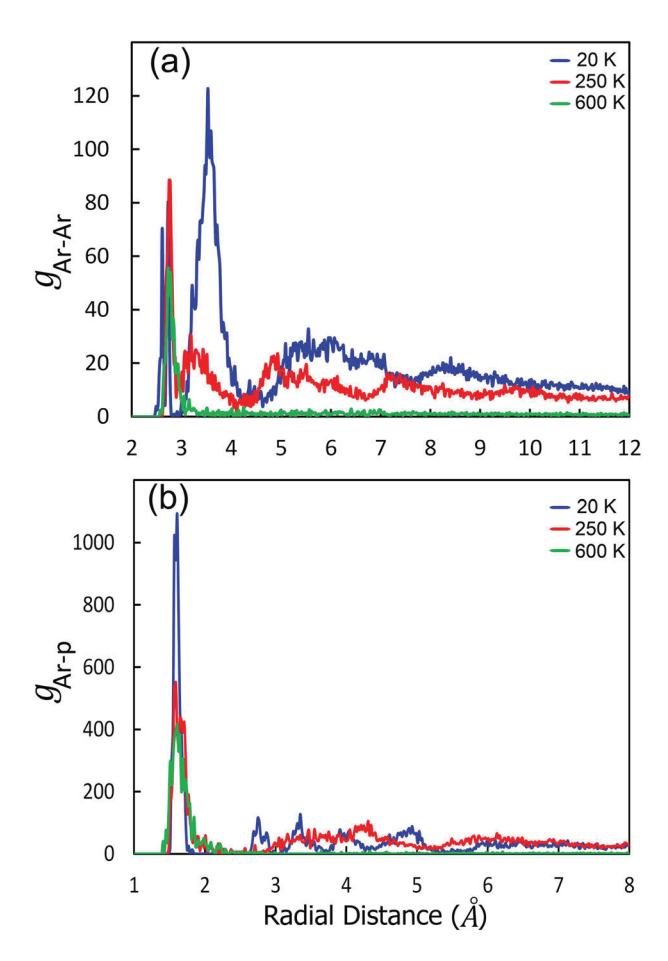


Figure 5. The pai–correlation (RDF) curves for (a) Ar–Ar, and (b) Ar–p distributions at various temperatures at argon density 10^{21} cm⁻³, and proton density 10^{20} cm⁻³. The characteristic peaks for the solid, liquid and gas phases are distinctly visible at T=20, 250 and 600 K, respectively. In addition to RDF, we also use the size of the cluster (the number of Ar atoms in the cluster) to distinguish the appearance of different phases.

for the solid structures (also indicated in Figure 2(b)). The red curve at $T=250\,\mathrm{K}$ illustrates a similar sharp peak, followed by a few smaller subsequent peaks. The absence of exact intervals in between these peaks is an indication of a loosely packed structure, which is a known feature in liquids. Due to increased mobility, atoms in the liquid state do not maintain a constant structure. Since particles become independent of each other at large distances, their RDF do not maintain long range order, and the distribution returns to the bulk density. Finally, the single peak in the green curve at $T=600\,\mathrm{K}$ with a rapidly decaying form is the characteristic feature of the gas phase. Similar features appear in Figure 5(b) for the Ar–p RDF curves.

Visualisation of the final configurations in the gas phase shows the existence of a tetrahedral-like structure with a proton at the centre. This structure which is relatively stable up to the highest temperatures we simulated, i.e. T=800 K, may be an indication for the coordination number ~ 4 for the p–Ar system.

The behaviour of the RDF with temperature, combined with the cluster size (number of Ar atoms in the cluster) pattern in Figure 3, confirms how the long range order changes in the cluster with increasing *T*, leading to the transition through different phases, when seeded with protons.

3.4. Critical temperature for protonated clusters

The proton interaction with Ar atoms and proton–proton correlation significantly contribute to the formation of stable proton–argon clusters. The charge screening, a specific type of correlation effects, reduces the total energy of the Ar–p clusters and makes them more stable. We consider a neutral proton and electron plasma in the Ar bath gas. The Debye screening length, λ_D , depends mostly on the proton density and temperature,

$$\lambda_D \simeq \sqrt{\frac{\varepsilon_0 k_{\rm B} T_p}{q_p^2 \rho_p}} \Leftrightarrow k_{\rm B} T_p = 4\pi \left(\frac{q_p^2}{4\pi \, \varepsilon_0 \lambda_D}\right) \rho_p \lambda_D^3,$$
 (9)

where T_p , q_p , ρ_p are the temperature, charge and the number density of protons in the simulation cell, respectively.

The efficiency of the Debye screening depends on the number of free charged particles $n_p \sim \rho_p \lambda_D^3$ inside a sphere with the Debye length λ_D . The characteristic energy of the screened Coulomb interaction $q_p^2/4\pi \varepsilon_0 \lambda_D$ can be used to estimate the correlation energy $\varepsilon_D =$ $\xi q_p^2/4\pi \varepsilon_0 \lambda_D$ of the charged particles interaction. The correction parameter $\xi(\rho_p, \rho_{Ar}, T_p)$ depends on the configuration of Ar-p clusters and on the relative strength of Ar-p, Ar-Ar and p-p interactions. ξ -values may be slightly different for the liquid, amorphous or crystalline structures. For systems with relatively large proton density, the correction parameter $\xi \sim 1$, but at low proton densities ξ -coefficient may be an order of magnitude larger. The physical reason for this is a relatively strong Ar-p attraction, compared to the screened p-p repulsion at small values of ρ_p .

At low charge densities the Coulomb correlation energy depends rather on the cluster radius ($\varepsilon_D \sim q_p^2/4\pi\,\varepsilon_0 R_p$), as well as the number of protons in the cluster ($n_p \sim \rho_p R_p^3$). Our MD simulations show that the radius of the Ar-p critical clusters varies in a relatively narrow interval $R_p=11$ –15 Å even when the proton density is altered in a broad interval of $\rho_p \sim 10^{18}$ – 10^{20} cm⁻³. In the numerical MD simulations of the cluster stability, the density of free protons is $\rho_p=N_p/L^3$, when the simulation box length is L=100 Å.

The correlation energies are especially important for the critical states of liquid/amorphous Ar-p clusters, where a relative small increase in temperature, or screening length, leads to the cluster evaporation. The simplified relationship between the critical temperature, T_{crit} (the highest temperature at which stable clusters still exist), and the critical proton densities, ρ_{p_c} , can be formulated using Equation (3). The fragmentation of Ar-p clusters may occur, if the average thermal energy $\frac{3}{2}k_BT_{crit}$ is larger than the proton correlation energy in the cluster $n_p\varepsilon_D$ or larger than the binding energies induced by Ar-p and Ar-Ar interactions. The model equation for the simplified relationship between T_{crit} and n_p in our analysis of the Ar-p clusters can be written as

$$T_{crit} = \frac{8\pi}{3} \xi \left(\frac{q_p^2}{4\pi \varepsilon_0 \lambda_D k_{\rm B}} \right) \times \left(\frac{\lambda_D}{L} \right)^3 N_p + T_{\rm crit}^{\rm Ar}, (10)$$

where $T_{\rm crit}^{\rm Ar} \simeq 108~{\rm K}$ is the critical temperature for Arclusters in the pure Ar gas obtained in our numerical simulations. Numerical values $\xi(N_p,T_{\rm crit})$ of the correction coefficient,

$$\xi = \xi(n_p, T_{\text{crit}}) \simeq 0.12 \frac{R_p(n_p, T_{\text{crit}})}{\lambda_D(n_p, T_{\text{crit}})}$$
(11)

have been computed using R_p -data from the MD simulations of Ar-p cluster formation. Equation (10) can be considered as a transcendental equation for self-consistent calculations of the critical temperatures, $T_{\rm crit}$. Comparisons between critical temperatures calculated from the analytical formula, Equation (10), and computed in our MD simulations are shown in the inset of Figure 3. Agreement is excellent for high proton densities. Nevertheless, for a small number of protons the results of MD simulations and prediction of analytical formula differ about $\sim 10-15\%$ because averaged Ar-p and Ar-Ar interactions dominate over an average value of p-p repulsive energy.

3.5. Clustering at lower density

Finally, we performed simulations at a lower argon density, 10^{20} cm⁻³. This density is generated by increasing the size of the square simulation box to the length of 215.44 Å, while the number of argon atoms are kept constant at 1000. Figure 6 shows the change of the average cluster size with respect to temperature for different proton contributions. As can be seen in this figure, transition to the gas phase for the case of pure argon (red dotted curve) occurs at around $T = 100 \, \text{K}$, compared to $T = 120 \, \text{K}$ when the density of argon was $10^{21} \, \text{cm}^{-3}$. We have found that adding protons in the lower density Ar gas pushes the transition to the gas phase to

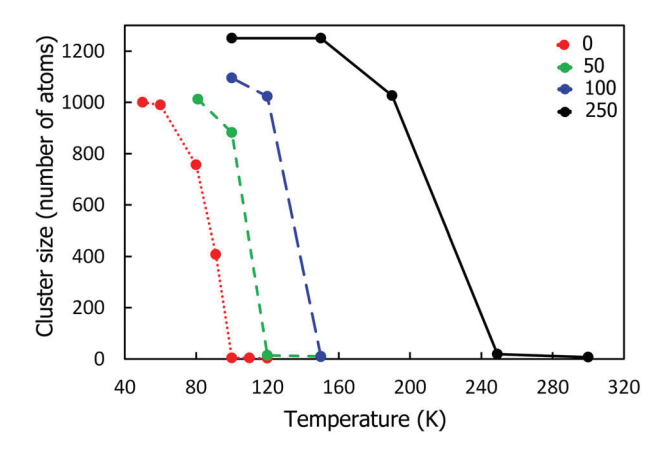


Figure 6. The size of Ar clusters against temperature over a range of proton densities, when the initial argon density is 10^{20} cm⁻³ for an increasing number of protons: 0, 50, 100 and 250.

higher temperatures. At the same time, no liquid phase plateau forms even at the highest number of protons we simulated, i.e. $N_p = 250$. This is because the Debye length increases at low densities to become greater than the distance of the Ar–p interaction where is the most attractive.

4. Summary and outlook

Extensive molecular dynamics simulations employed to understand the formation of the critical argon nanoclusters under different conditions. We showed that the short-term nucleation and aggregate formation are enhanced when the Ar bath gas are seeded with proton. The effectiveness of the seeding mechanism was evaluated at different argon densities and temperatures. In particular, we observed the formation of stable liquid droplets over a wide range of (up to around $T = 500 \,\mathrm{K}$) when a $10^{21} \,\mathrm{cm}^{-3}$ argon sample is protonated. The phase transition of such proton mediated argon clusters was analysed by studying the paircorrelation (radial distribution functions) at different temperatures to confirm the solid, liquid and gaseous nature of each phase. The comparison of constant pressure phase transition lines suggest a linear increase of the temperature at which the clusters dissolve into the gas phase with increasing proton density. This indicates the efficiency of the proton seeding process to enhance the stability of the formed critical nanoclusters at higher temperatures.

Further work will attempt to improve the model beyond considering purely binary interactions between particles. We plan to include few-body molecular potentials to more accurately depict the long range attraction between an argon and a proton–argon cluster containing a few argon atoms. Modelling of haze and



dust nanoparticle formation in astrophysical and atmospheric environments from water vapour, methane, or other organic molecules may be considered as a next logical step of investigations.

Acknowledgements

OCFB was supported through a collaborative program between Southampton University and Harvard-Smithsonian Center for Astrophysics program. HRS acknowledges support from the NSF through a grant for ITAMP at Harvard University. One of the authors (DV) is also grateful for the support received from the National Science Foundation through grants PHY-1831977 and HRD-1829184.

Disclosure statement

No potential conflict of interest was reported by the author(s).

Funding

This work was supported by National Science Foundation, Division of Human Resource Development [1829184] and Division of Physics [1831977]. OCFB was supported through a collaborative program between Southampton University and Harvard-Smithsonian Center for Astrophysics program. HRS acknowledges support from the NSF through a grant for ITAMP at Harvard University. One of the authors (DV) is also grateful for the support received from the National Science Foundation through grants PHY-1831977 and HRD-1829184.

ORCID

D. Vrinceanu http://orcid.org/0000-0002-8820-9073 H. R. Sadeghpour http://orcid.org/0000-0001-5707-8675

References

- [1] W.S. Hopkins, Mol. Phys. 113 (21), 3151-3158 (2015).
- [2] A.W. Castleman and R.G. Keesee, Science 241 (4861), 36-42 (1988).
- [3] R. Alayan, L. Arnaud, A. Bourgey, M. Broyer, E. Cottancin, J.R. Huntzinger, J. Lerme, J.L. Vialle, M. Pellarin and G. Guiraud, Rev. Sci. Instrum. 75 (7), 2461-2470
- [4] R. Alayan, L. Arnaud, M. Broyer, E. Cottancin, J. Lermé, J.L. Vialle and M. Pellarin, Phys. Rev. B 73, 125444 (2006).
- [5] Z. Felfli, T. Karman, V. Kharchenko, D. Vrinceanu, J.F. Babb and H.R. Sadeghpour, Mon. Not. R. Astron. Soc. 482 (1), 1330-1337 (2019).
- [6] X. Zhang, D.F. Strobel and H. Imanaka, Nature 551, 352 (2017).
- [7] L.D. Deming and S. Seager, J. Geophys. Res. 122 (1), 53–75
- [8] D. Vrinceanu, S. Kotochigova and H.R. Sadeghpour, Phys. Rev. A 69, 022714 (2004).
- [9] J.J. Spake, D.K. Sing, T.M. Evans, A. Oklopcic, V. Bourrier, L. Kreidberg, B.V. Rackham, J. Irwin, D. Ehrenreich, A. Wyttenbach, H.R. Wakeford, Y. Zhou, K.L. Chubb, N.

- Nikolov, J.M. Goyal, G.W. Henry, M.H. Williamson, S. Blumenthal, D.R. Anderson, C. Hellier, D. Charbonneau, S. Udry and N. Madhusudhan, Nature 557 (7703), 68-70 (2018).
- [10] J. Szudy and W.E. Baylis, Phys. Rep. 266 (3), 127-227 (1996).
- [11] N. Allard and J. Kielkopf, Rev. Mod. Phys. 54, 1103-1182 (1982).
- [12] S.M. Hörst, C. He, N.K. Lewis, E.M.R. Kempton, M.S. Marley, C.V. Morley, J.I. Moses, J.A. Valenti and V. Vuitton, Nat. Astron. 2 (4), 303-306 (2018).
- [13] S.M. Hörst and M.A. Tolbert, Astrophys. J. 770 (1), L10 (2013).
- [14] F. Pauzat, Y. Ellinger, O. Mousis, M.A. Dib and O. Ozgurel, Astrophys. J.777 (1), 29 (2013).
- [15] M. Gatchell, P. Martini, L. Kranabetter, B. Rasul and P. Scheier, Phys. Rev. A 98, 022519 (2018).
- [16] K. Shen, A. Wucher and N. Winograd, J. Phys. Chem. C 119 (27), 15316-15324 (2015).
- [17] C.J. Stephan and R.C. Fortenberry, Mon. Not. R. Astron. Soc. 469 (1), 339-346 (2017).
- [18] R.C. Fortenberry, ACS Earth Space Chem. 1 (1), 60-69 (2017).
- [19] P. Schilke, D.A. Neufeld, H.S.P. Müller, C. Comito, E.A. Bergin, D.C. Lis, M. Gerin, J.H. Black, M. Wolfire, N. Indriolo, J.C. Pearson, K.M. Menten, B. Winkel, Á. Sánchez-Monge, T. Möller, B. Godard and E. Falgarone, A&A 566, A29 (2014).
- [20] V.E. Bondybey and G.C. Pimentel, J. Chem. Phys. 56 (8), 3832-3836 (1972).
- [21] H.M. Kunttu and J.A. Seetula, Chem. Phys. 189 (2), 273-292 (1994).
- [22] D.C. McDonald, D.T. Mauney, D. Leicht, J.H. Marks, J.A. Tan, J.L. Kuo and M.A. Duncan, J. Chem. Phys. 145 (23), 231101 (2016).
- [23] K.T. Giju, S. Roszak and J. Leszczynski, J. Chem. Phys. 117 (10), 4803–4809 (2002).
- [24] M. Beyer, A. Lammers, E.V. Savchenko, G. Niedner-Schatteburg and V.E. Bondybey, Phys. Chem. Chem. Phys. 1, 2213-2221 (1999).
- [25] T. Kraska, J. Chem. Phys. 124 (5), 054507 (2006).
- [26] K. Laasonen, S. Wonczak, R. Strey and A. Laaksonen, J. Chem. Phys. 113 (21), 9741-9747 (2000).
- [27] V.V. Hoang and T. Odagaki, Phys. Rev. B 77, 125434 (2008).
- [28] L. Ming, N. Markovic, M. Svanberg and J.B.C. Pettersson, J. Phys. Chem. A 101 (22), 4011–4018 (1997).
- [29] R.S. Dumont, S. Jain and A.G. Basile, J. Chem. Phys. 102 (10), 4227–4238 (1995).
- [30] C. Rey, L. Gallego, M. Iniguez and J. Alonso, Phys. B 179 (4), 273–277 (1992).
- [31] F. Baletto and R. Ferrando, Rev. Mod. Phys. 77, 371-423
- [32] O.G. Danylchenko, S.I. Kovalenko and V.N. Samovarov, Low Temp. Phys. 30 (2), 166-170 (2004).
- [33] A.G. Danil'chenko, S.I. Kovalenko and V.N. Samovarov, Low Temp. Phys. 34 (11), 966-968 (2008).
- [34] O.G. Danylchenko, S.I. Kovalenko, O.P. Konotop and V.N. Samovarov, Low Temp. Phys. 40 (12), 1083-1086
- [35] B. Li, G. Qian, A.R. Oganov, S.E. Boulfelfel and R. Faller, J. Chem. Phys. 146 (21), 214502 (2017).



- [36] A. Rytkanen, S. Valkealahti and M. Manninen, J. Chem. Phys. **108** (14), 5826–5833 (1998).
- [37] E.M. Lifshitz and L.P. Pitaevskii, *Physical Kinetics*, 3rd ed. (Elsevier, Oxford, 2010).
- [38] S. Plimpton, J. Comput. Phys. 117 (1), 1-19 (1995).
- [39] W. Humphrey, A. Dalke and K. Schulten, J. Mol. Graph. **14** (1), 33–38 (1996).
- [40] J.A. White, J. Chem. Phys. 111 (20), 9352-9356 (1999).
- [41] M. Henderson and M.S. Wertheim, J. Chem. Phys. **51** (12), 5420–5429 (1969).
- [42] V. Sidis, J. Phys. B 5 (8), 1517–1528 (1972).
- [43] J.D. Jackson, *Classical Electrodynamics*, 2nd ed. (John Wiley & Sons, New York, 1975).
- [44] T. Andersen, Phys. Rep. 394 (20), 157–313 (2004).
- [45] K. Hermann, Crystallography and Surface Structure: An Introduction for Surface Scientists and Nanoscientists

- (John Wiley & Sons, Ltd., Weinheim, Germany, 2011), p. 266.
- [46] D. Chandler, *Introduction to Modern Statistical Mechanics* (Oxford University Press, New York, 1987).
- [47] K.O. Christe, Angew. Chem. Int. Ed. 40 (8), 1419–1421 (2001).
- [48] P. Van't Zelfde, M. Omar, H. LePair-Schroten and Z. Dokoupil, Physica (Amsterdam) 38, 241 (1968).
- [49] A.L. Gossman, R.D McCarty and J.G. Hust, Nat. Stand. Ref. Data Ser. Nat. Bur. Stand. NSRDS-NBS 27, 1–146 (1969).
- [50] D. Bolmatov, M. Zhernenkov, D. Zavayalov, S.N. Tkachev, A. Cunsolo and Y.Q. Cai, Sci. Rep. 5, 15850 (2015).
- [51] U. Rössler, *Solid State Theory: An Introduction* (Springer-Verlag, Berlin, 2009), p. 12.